Surface-to-space atmospheric waves from Hunga Tonga-Hunga Ha'apai eruption

Corwin J Wright*[1], Neil P Hindley[1], M Joan Alexander[2], Mathew Barlow[3], Lars Hoffmann[4], Cathryn N Mitchell[1], Fred Prata[5,6], Marie Bouillon[7], Justin Carstens[8], Cathy Clerbaux[7], Scott M Osprey[9], Nick Powell[10], Cora E Randall[11,12], and Jia Yue[13,14]

1. Centre for Space, Atmospheric and Oceanic Science, University of Bath, Bath, UK
2. Northwest Research Associates, Boulder, Colorado, USA
3. Environmental, Earth & Atmospheric Sciences, University of Massachusetts Lowell, Massachusetts, USA
4. Jülich Supercomputing Center, Forschungszentrum Jülich, Jülich, Germany
5. AIRES, Mt Eliza, Victoria, Australia
6. School of Electrical Engineering, Computing & Mathematical Science, Curtis University, Western Australia
7. LATMOS/IPSL, Sorbonne Université, UVSQ, CNRS, Paris, France
8. Center for Space Science and Engineering Research, Bradley Department of Electrical and Computer Engineering, Virginia Tech, Blacksburg, VA, USA
9. Atmospheric, Oceanic and Planetary Physics, Department of Physics, University of Oxford, Oxford, UK
10. Raytheon Technologies
11. Laboratory for Atmospheric and Space Physics, University of Colorado Boulder, Boulder, CO, USA
12. Department of Atmospheric and Oceanic Sciences, University of Colorado Boulder, Boulder, CO, USA
13. NASA Goddard Space Flight Center, Community Coordinated Modeling Center, Greenbelt, MD, USA
14. Physics Department, Catholic University of America, Washington, DC, USA
* Corresponding author, c.wright@bath.ac.uk

Abstract

The January 2022 Hunga Tonga–Hunga Ha'apai eruption was one of the most explosive volcanic events of the modern era[1,2], producing a vertical plume which peaked > 50km above the Earth[3]. The initial explosion and subsequent plume triggered atmospheric waves which propagated around the world multiple times[4]. A global-scale wave response of this magnitude from a single source has not previously been observed. Here we show the details of this response, using a comprehensive set of satellite and ground-based observations to quantify it from surface to ionosphere. A broad spectrum of waves was triggered by the initial explosion, including Lamb waves[5,6] propagating at phase speeds of 318.2±6 ms^{-1} at surface level and between 308±5 to 319±4 ms^{-1} in the stratosphere, and gravity waves[7] propagating at 238±3 to 269±3 ms^{-1} in the stratosphere. Gravity waves at sub-ionospheric heights have not previously been observed propagating at this speed or over the whole Earth from a single source[8,9]. Latent heat release from the plume remained the most significant individual gravity wave source worldwide for >12 hours, producing circular wavefronts visible across the Pacific basin in satellite observations. A single source dominating such a large region is also unique in the observational record. The Hunga Tonga eruption represents a key natural experiment in how the atmosphere responds to a sudden point-source-driven state change, which will be of use for improving weather and climate models.

On the 15th of January 2022, the Hunga Tonga–Hunga Ha'apai submarine volcano (20.54°S, 175.38°W, hereafter 'Hunga Tonga') erupted, producing a vertical plume >30 km tall with overshooting tops above 55 km, a record in the satellite era[3] and likely longer[2]. From surface-pressure data, we estimate a single-event energy release from the initial explosion of between 10 and 28 EJ, likely larger than the 1991 Mt Pinatubo eruption[2] (~10 EJ), and possibly comparable to Krakatoa in 1883[2] (~30 EJ) (see Methods and Extended Data Figures 1a,b).

Large explosions such as volcanoes and nuclear tests are theoretically understood to produce atmospheric waves[10,11] across a range of length and frequency scales. At horizontally-short wavelengths, these include external Lamb waves[5,6,12] , acoustic waves[11] and internal gravity waves[13]. In addition to explosion-generated waves, volcanoes can also act as a sustained wave source after the initial eruption via updrafts and heating associated with plume convection[14,15].

In practice, observations of such waves at sub-acoustic frequencies after volcanic eruptions are rare. Krakatoa[6] and Pinatubo[16], amongst others, produced strong Lamb waves visible in surface pressure. Internal waves in the boundary layer have been inferred from seismography, barometry and infrasound for eruptions including El Chichon[14] (1982), Pinatubo[14] and Okmok[15] (2008). In the free atmosphere, local gravity wave activity associated with plume convection has been seen in mesospheric nightglow over the La Soufrière (2021) and Calbuco[13] (2015) eruptions and in local cloud over eruptions including Cumbre Vieja (2021). Re-examination of 1990s Advanced Very High Resolution Radiometer data also shows waves in cloud above Pinatubo (Extended Data Figure 2). Finally, an electron-density ionospheric wave response is usually observed[17-21], with the response magnitude proposed as a metric of volcano explosive power[22].

There is however no direct observational evidence for long-distance propagation in the free electrically-neutral atmosphere of either Lamb or gravity waves triggered by volcanoes. Pre-2000s satellite observations had insufficient resolution and coverage to measure such waves, and no event since[8] has produced a wave response similar to that identified within hours[23] of Hunga Tonga. This eruption thus represents an opportunity to quantify the wave response to a point-source disruption at a scale and comprehensiveness unique in the observational record.

Eruption and Immediate Wave Response

Figures 1 and 2 show the propagation of Lamb and gravity waves triggered by the initial eruption on the 15th of January, Figure 1 as height-integrated data from the Geostationary Operational Environmental Satellite (GOES) and MeteoSat platforms and Figure 2 as height-resolved measurements from multiple instrument types in addition to GOES.

The eruption became visible just before 04:00 UTC as a plume which reached a width of 200km and height of >30km within 30 minutes[3]. 20-30 minutes after the plume began rising, an atmospheric wave became visible in ten-minute-resolution near-infrared geostationary imagery. Back-projection from surface pressure data shows that the trigger source occurred at 04:28±0:02 UTC, with the leading wavefront propagating away at a near-surface phase speed of 318.2±6 ms^{-1} (Figure 2c, Extended Data Figure 1c,d, Supplementary Figure 1). Based on the high phase speed, large amplitude and non-dispersive nature of the signal we identify this as a Lamb wave. This type of wave is non-dispersive, and the observed speed is consistent with the Lamb wave produced by Krakatoa, estimated[24] to have propagated at 318.8±3 ms^{-1}.

The Hunga Tonga Lamb wave propagated around the globe, passing through the antipodal point in Algeria 18.1 hours (±7.5 minutes) after the eruption (Figure 1). By this time, the wavefront had deformed due to atmospheric and surface processes, and passed through the antipode as four distinct wavefronts (Figure 1m-p). Over the following days, it was tracked propagating at least three times[25,4] around the Earth. We also see a faint signal in GOES data consistent with the wave being partially reflected from the Andes on its first transit (Figure 1), and evidence of the wave being slowed over South America (Extended Data Figure 10).

Using radiance data from the Atmospheric Infrared Sounder (AIRS), Cross-track Infrared Sounder (CrIS) and Infrared Atmospheric Sounding Interferometer (IASI) polar-orbiting thermal infrared (IR) sounders (specifically, 4.3µm data sensitive to altitudes ~39 km±5 km and 15 µm data sensitive to the both ~25±5km and ~42±5km altitude levels separately, Figure 2a), we see the Lamb wave as a high-amplitude monochromatic pulse with a phase speed of between 308±5 and 319±4 ms^{-1} depending on location. We also observe it as a pulse just above the noise floor of Cloud Imaging and Particle Size (CIPS) Rayleigh albedo anomaly data 12 300km away from and 10.75 hours after the eruption (~55±5km altitude, phase speed 316-319 ms^{-1}, Extended Data Figure 4a), and as phase fronts in hydroxyl airglow over Hawai'i, 4960 km away from and 4.3 hours after (~87±4km altitude, phase speed 318 ms^{-1}).

The observed Lamb wave phase fronts are uniform in height and phase speed to within the error range of each instrument from the surface to at least the upper mesosphere/lower thermosphere. The energy density of a Lamb wave is theoretically expected[26] to decay exponentially with height, and the observed phase speed is consistent with a vertical mean of sound speed weighted according to this energy distribution (see Methods). Our data may show evidence of a slightly different speed for propagation in different directions across the Earth (e.g. at Broome, Australia, we measure 319 ms^{-1} for the westward-travelling wave and 316 ms^{-1} for the eastward, Extended Data Figure 1e), but this is within the uncertainty range of our measurements. The asymmetric perturbations we observe are consistent in sign with such a shift due to background winds.

Following the Lamb wave, we observe a series of slower waves with continually varying speeds and horizontal wavelengths (λ_h) that we identify as a dispersive packet of fast internal gravity waves (Figure 2a). These have phase speeds of 240-270 ms^{-1}, varying with local λ_h. The leading phase front has the largest amplitude and longest λ_h, with a brightness temperature (BT) amplitude of 0.74 K and λ_h of 380 km here falling to 0.15 K and 100 km across the packet width. This packet is observed to extend ~2000 km and eight phase cycles across the South Pacific ~7 hours after generation (Extended Data Figure 5). We observe the packet over multiple orbits of AIRS, CrIS, and IASI across the globe, in CIPS over Antarctica, and in airglow (~85km altitude, depth ~8km) above Hawai'i. Vertical wavelength (λ_z) is poorly defined but very deep: no phase difference is seen between AIRS observations at 25 and 42 km altitude, and calculations based on observed speed and λ_h imply $\lambda_z >> 110$ km, i.e. greater than the depth of the homosphere. These phase speeds are consistent with vertically-propagating gravity waves travelling at speeds close to, but very slightly less than, the theoretical maximum speeds achievable prior to total internal reflection (See Methods and Extended Data Figure 6) and with the same temporal origin and source as the Lamb wave.

This leading gravity wave packet passes through the antipode at times between ~00:30 and 02:30 UTC on the 16th of January, i.e. 20-22 hours after the eruption (Extended Data Figures 7a-c), with the broad time window determined by separation of different λ_h components with time. Gravity waves remaining coherent and expanding over the whole globe from a single source of any kind are unprecedented in the observational record[8]. On their return journey from the antipode, the waves become difficult to distinguish in our intermittent low-Earth orbit satellite snapshots from those produced both later by Hunga Tonga and by other sources, and consequently we cannot track them to their extinction.

The gap between the initial Lamb wave and subsequent gravity wave grows with time. This is consistent with a theoretically-predicted forbidden phase speed range between external Lamb wave and internal gravity wave limits imposed by total internal reflection (Extended Data Figure 6). Two low-amplitude wavefronts are present in the gap; these propagate with the same speed as the leading Lamb wavefront, but trace back to different origin times (Figure 2a and Extended Data Figure 4b). We therefore identify these as Lamb waves triggered by subsequent smaller explosions which were also observed in local surface pressure (Extended Data Figure 8).

Ionospheric data (Figure 2d and Extended Data Figure 3) show key differences from the lower atmosphere. Over New Zealand, we see three large travelling ionospheric disturbances (TIDs), with phase speeds, λ_h and amplitudes of (1) 667 ms^{-1}, 1000 km, 0.1 TEC Units (TECu); (2) 414 ms^{-1}, 700 km, 0.4 TECu and (3) 343 ms^{-1}, 400 km and >0.3 TECu respectively. The speed and propagation direction of these waves is consistent with a Hunga Tongan source between 04:15 and 05:00, but do not share the arrival time, phase speed or λ_h of the Lamb wave in other atmospheric layers. Therefore, we do not identify these TIDs as the Lamb wave. However, a strong and brief TEC modulation, spiking at an amplitude of >0.6 TECu, is seen at 06:15 consistent with the expected arrival time and brief period of the Lamb wave.

We do not see TID 1 over North America, but do see a signal consistent with TID 2 and another TID (4) with phase speed ~311 m/s which is consistent with a later surface pressure perturbation measured over Tonga. We again see a strong TEC modulation at the expected Lamb wave arrival time.

The properties of TIDs 1 and 2 are inconsistent with slant path gravity waves propagating from Hunga Tonga, but these TIDs could have reached the observed sites by indirect paths, e.g. by vertically propagating as acoustic or gravity waves above the volcano then travelling at high horizontal speeds through the ionosphere. The properties of TIDs 3 and 4 are consistent with the wave activity generated over Hunga Tonga in the hours after the primary eruption.

Sustained Post-Eruption Wave Generation

After the initial trigger, sustained gravity wave generation is seen in the clouds above Hunga Tonga and radiating outwards across the Pacific basin. While smaller in amplitude and slower in phase speed than those from the initial eruption, these waves are also highly anomalous relative to past gravity wave observations.

Figure 3 shows BT measurements from (a-d) the GOES 10.3µm channel over the Hunga Tonga area and (e-g) the AIRS, CrIS and IASI 4.3µm stratospheric channels over the Pacific basin for selected times.

In GOES observations of the eruption cloud top (Figure 3a-c, Supplementary Figure 3), arced features consistent in morphology and temporal progression with propagating concentric gravity wave phase fronts are visible. λ_h ranges from the 3km resolution limit of the data to 65km, and BT amplitude from 0.5-8K. These measured properties are very similar to those of gravity waves generated near the convective centres of hurricanes.

The apparent centre of these waves is slightly west of Hunga Tonga. This is consistent with refraction of the wave field by the prevailing easterly winds. The waves are remarkably consistent in concentric shape over several hours, suggesting a powerful and relatively persistent pulsing source for wave generation. The source may be pulses of convection within the plume above the volcano. The waves weaken in amplitude over time, particularly after 15:00UTC, but are visible until at least 19:20 UTC (Figure 3d). They are not found on subsequent days. These results suggest that the volcano may have created a sustained source of convectively-generated waves for nearly fifteen hours after the initial eruption.

Stratospheric AIRS, CrIS and IASI observations (Figure 3e-g, Extended Data Figure 7d-o) show wave activity across a range of spatial, frequency and amplitude scales throughout the

Pacific basin, all centred on Hunga Tonga. Tracking individual phase fronts is challenging as these data are near-instantaneous at any given location, but conservatively the distribution must include waves with phase speeds >100 ms^{-1}. For example, small-scale continuous wavefronts centred on Hunga Tonga are clearly visible near Japan before 16:00 in Figure 3g and, even if emitted at the earliest possible time of 04.28 UTC, must have phase speeds ~200 ms^{-1} to have travelled this far. Unlike more typical observed waves, these waves can therefore propagate with little apparent influence from global wind patterns due to their unusually large phase speeds. Such fast speeds reduce normal dissipation effects, allowing the waves to propagate vast distances and affect much higher altitudes than typical gravity waves.

These waves dominate the stratospheric gravity wave spectrum over a radius >9000km for >12 hours (Extended Data Figure 7d-o). This is exceptional for a single source, and unique in our observational record[8,9]. Orographic wave sources often persist for longer, but are spatially localised; while some waves in the southern polar jet may have propagated downstream[27,28] or laterally [8,29] from orographic sources, the area they affect is an order of magnitude smaller than here and the waves themselves highly intermittent. Waves from non-orographic sources such as tropical convection and extreme events such as hurricanes, meanwhile, typically become indistinguishable from background within 2000-3500 km[30,31].

How were the waves generated?

Although we cannot directly observe the generation of the waves due to insufficient temporal resolution (for the initial explosion) and ash plume blocking effects (for both the initial explosion and subsequent wave generation), the observed wave properties and context allow us to infer likely mechanisms by which they were generated.

The strong initial response is likely due to the eruption's shallow submarine context and large explosive power. As the volcanic vent was only tens to hundreds of metres below water[32] the seawater did not suppress the blast but was instead flash-boiled[33] and propelled into the stratosphere. Here it condensed, releasing latent heat near-instantaneously across a depth of tens of kilometres. This strong and short-lived forcing would produce vertically-deep waves across a broad spectrum, consistent with observations. This mechanism is also consistent with significant and large IASI-observed increases in stratospheric water vapour (Extended Data Figure 9), and H_2SO_4 in the plume relative to what would be expected for an eruption of this size. This is in turn consistent with the speculation that, due to insufficient volcanogenic SO_2 and the time available to produce H_2SO_4 from SO_2, the observed H_2SO_4 was formed from SO_4^{2-} released from sea water.

Subsequent wave generation is likely due to similar processes as standard convective waves, such as mechanical oscillator effects[34] associated with vertical air motion within the plume or pulsing from the volcanic heat source below. Such forces would produce sufficiently strong perturbations to generate gravity waves visible both in the plume and propagating freely away. Such a mechanism is again consistent with our observations, particularly the similarity in morphology and amplitude of the observed waves to the concentric generated by hurricanes[35,36] and convective weather systems[31,37].

Another possibility is that the eruptive energy could have transferred to tsunami waves and the tsunamis in turn have generated the waves we observe[38]. However, we argue that this is less likely than simple linear propagation from a convective atmospheric source due to the highly regular concentric nature of the observed atmosphere waves in Figures 3e-g, which show no significant evidence of tsunami deformation effects. Other studies have shown that the atmospheric waves also generated meteotsunamis in both the Pacific and other basins[39,40], highlighting the complex interplays between ocean and atmospheric waves in the Earth system.

Weather/Climate Forecasting Implications

While in recent years we have been able to routinely characterise gravity waves in observational data, understanding how the observed spectrum at a given location arises has been complicated by fundamental problems in distinguishing the source of a wave from the pathway it has taken to the observation[28]. Being able to separate these problems would lead to major advances in simulating and parameterising gravity waves in next-generation weather and climate models. The Hunga Tonga eruption represents an important natural experiment in this area: the volcano was a clearly-identifiable near-point source, produced gravity waves across a broad range of spatiotemporal and frequency scales, and these waves were observed by a diverse constellation of instruments worldwide.

While the $\gtrsim 150 ms^{-1}$ phase speed waves produced by the initial eruption are unusual at heights below the mesosphere, models in current use do routinely parameterise gravity waves with phase speeds as high as $100\ ms^{-1}$ at altitudes as low as 16 km[41], similar to a large fraction of those we observe after the main eruption. In addition, waves in the poorly-instrumented mesosphere and above can routinely have speeds of hundreds of metres per second[42], and observations of what is an extreme case in the better-instrumented stratosphere could provide useful insight for research in this area.

As such, simulating this eruption in atmospheric models, whether as a point convective source or in a dedicated volcanic simulation, could provide major insight into the strengths and deficiencies of models operating across all levels of the atmospheric system. While current-generation global-scale weather models cannot reproduce these waves due to their relatively-limited spatial and temporal resolution and the Courant-Friedrichs-Lewy condition, the waves can be directly resolved by large eddy simulations[43] and similar specialist models[42], albeit only currently for relatively small geographic regions. For such models, the wave observations documented here, made possible only by the exceptional strength of the event, provides a rich source of data to simulate, parameterise, and understand these wave types, all of which will be of high relevance to weather and climate models.

Finally, we note that the observed propagation of these waves can also be used as a test of how well models reproduce the bulk atmosphere, by comparing propagation delays for the observed Lamb and gravity waves with those reproduced by simulated waves passing through the model atmosphere. These could provide important information quantifying how well current and future models represent atmospheric winds, temperatures and density structures, particularly if constrained to the initial conditions of the 15th of January 2022.

Main References

1. Poli, P. & Shapiro, N. M. Rapid characterization of large volcanic eruptions: measuring the impulse of the Hunga Tonga explosion from teleseismic waves. http://www.essoar.org/doi/10.1002/essoar.10510358.1 (2022) doi:10.1002/essoar.10510358.1.
2. Pyle, D. M. Sizes of Volcanic Eruptions. in The Encyclopedia of Volcanoes 263–269 (Elsevier, 2000).
3. Carr, J. L., Horvath, A., Wu, D. L. & Friberg, M. D. Stereo Plume Height and Motion Retrievals for the Record-Setting Hunga Tonga-Hunga Ha'apai Eruption of 15 January 2022. Geophys. Res. Lett. **49**, e2022GL098131 (2022)
4. Harrison, G. Pressure anomalies from the January 2022 Hunga Tonga-Hunga Ha'apai eruption. *Weather* **77**, 87–90 (2022).
5. Garrett, C. J. R. Atmospheric edge waves. Q.J Royal Met. Soc. **95**, 731–753 (1969).
6. The Eruption of Krakatoa and Subsequent Phenomena. Q.J.R. Meteorol. Soc. **14**, 301–307 (1888).
7. Fritts, D. C. & Alexander, M. J. Gravity wave dynamics and effects in the middle atmosphere. Rev. Geophys. **41**, 1003 (2003).
8. Hindley, N. P., Wright, C. J., Hoffmann, L., Moffat-Griffin, T. & Mitchell, N. J. An 18-Year Climatology of Directional Stratospheric Gravity Wave Momentum Flux From 3-D Satellite Observations. Geophys. Res. Lett. **47**, (2020).
9. Ern, M. et al. GRACILE: a comprehensive climatology of atmospheric gravity wave parameters based on satellite limb soundings. Earth Syst. Sci. Data **10**, 857–892 (2018).
10. Press, F. & Harkrider, D. Air-Sea Waves from the Explosion of Krakatoa. Science **154**, 1325–1327 (1966).
11. Pfeffer, R. L. & Zarichny, J. Acoustic-Gravity Wave Propagation from Nuclear Explosions in the Earth's Atmosphere. J. Atmos. Sci. **19**, 256–263 (1962).
12. Kanamori, H. & Given, J. W. Lamb pulse observed in nature. Geophys. Res. Lett. **10**, 373–376 (1983).
13. Miller, S. D. et al. Upper atmospheric gravity wave details revealed in nightglow satellite imagery. Proc Natl Acad Sci USA **112**, E6728–E6735 (2015).
14. Widmer, R. & Zürn, W. Bichromatic excitation of long-period Rayleigh and air waves by the Mount Pinatubo and El Chichon volcanic eruptions. Geophys. Res. Lett. **19**, 765–768 (1992).
15. De Angelis, S., McNutt, S. R. & Webley, P. W. Evidence of atmospheric gravity waves during the 2008 eruption of Okmok volcano from seismic and remote sensing observations: Gravity Waves at Okmok Volcano. Geophys. Res. Lett. **38** (2011).
16. Watada, S. & Kanamori, H. Acoustic resonant oscillations between the atmosphere and the solid earth during the 1991 Mt. Pinatubo eruption. J. Geophys. Res. **115**, B12319 (2010).
17. Astafyeva, E. Ionospheric Detection of Natural Hazards. Rev. Geophys. 2019RG000668 (2019) doi:10/gghhwc.
18. Themens, D. R. et al. Global propagation of ionospheric disturbances associated with the 2022 Tonga Volcanic Eruption. Geophys. Res. Lett. **49** e2022GL098158 (2022), doi: 10.1029/2022GL098158
19. Roberts, D. H., Klobuchar, J. A., Fougere, P. F. & Hendrickson, D. H. A large-amplitude traveling ionospheric disturbance produced by the May 18, 1980, explosion of Mount St. Helens. *J. Geophys. Res.* **87**, 6291 (1982).
20. Liu, C. H. *et al.* Global dynamic responses of the atmosphere to the eruption of Mount St. Helens on May 18, 1980. *J. Geophys. Res.* **87**, 6281 (1982).

21. Igarashi, K. *et al.* Ionospheric and atmospheric disturbances around Japan caused by the eruption of Mount Pinatubo on 15 June 1991. *Journal of Atmospheric and Terrestrial Physics* **56**, 1227–1234 (1994).
22. Manta, F. et al. Correlation Between GNSS-TEC and Eruption Magnitude Supports the Use of Ionospheric Sensing to Complement Volcanic Hazard Assessment. J Geophys Res Solid Earth **126**, (2021).
23. Adam, D. Tonga volcano eruption created puzzling ripples in Earth's atmosphere. Nature d41586-022-00127–1 (2022) doi:10/gn8ktd.
24. Taylor, G. I. Waves and tides in the atmosphere. Proc. R. Soc. Lond. A **126**, 169–183 (1929).
25. Lin, J.-T. et al. Rapid Conjugate Appearance of the Giant Ionospheric Lamb Wave in the Northern Hemisphere After Hunga-Tonga Volcano Eruptions. http://www.essoar.org/doi/10.1002/essoar.10510440.1 (2022) doi:10.1002/essoar.10510440.1.
26.Bretherton, F. P. Lamb waves in a nearly isothermal atmosphere. Q.J Royal Met. Soc. 95, 754–757 (1969).
27. Hindley, N. P., Wright, C. J., Smith, N. D. & Mitchell, N. J. The southern stratospheric gravity wave hot spot: individual waves and their momentum fluxes measured by COSMIC GPS-RO. Atmos. Chem. Phys. **15**, 7797–7818 (2015).
28. Wright, C. J., Hindley, N. P., Hoffmann, L., Alexander, M. J. & Mitchell, N. J. Exploring gravity wave characteristics in 3-D using a novel S-transform technique: AIRS/Aqua measurements over the Southern Andes and Drake Passage. Atmos. Chem. Phys. **17**, 8553–8575 (2017).
29. Plougonven, R., la Cámara, A., Hertzog, A. & Lott, F. How does knowledge of atmospheric gravity waves guide their parameterizations? Q.J.R. Meteorol. Soc **146**, 1529–1543 (2020).
30. Wright, C. J. Quantifying the global impact of tropical cyclone-associated gravity waves using HIRDLS, MLS, SABER and IBTrACS data. Q.J.R. Meteorol. Soc. **145**, 3023–3039 (2019).
31. Stephan, C. & Alexander, M. J. Realistic simulations of atmospheric gravity waves over the continental U.S. using precipitation radar data. J. Adv. Model. Earth Syst. **7**, 823–835 (2015).
32. Colombier, M. et al. Vesiculation and Quenching During Surtseyan Eruptions at Hunga Tonga-Hunga Ha'apai Volcano, Tonga. J. Geophys. Res. Solid Earth **123**, 3762–3779 (2018).
33. Witze, A. Why the Tongan eruption will go down in the history of volcanology. Nature d41586-022-00394-y (2022) doi:10/gpfhcm.
34. Fovell, R., Durran, D. & Holton, J. R. Numerical Simulations of Convectively Generated Stratospheric Gravity Waves. J. Atmos. Sci. **49**, 1427–1442 (1992).
35. Hoffmann, L., Wu, X. & Alexander, M. J. Satellite Observations of Stratospheric Gravity Waves Associated With the Intensification of Tropical Cyclones. *Geophys. Res. Lett.* **45**, 1692–1700 (2018).
36. Tratt, D. M. *et al.* GHOST: A Satellite Mission Concept for Persistent Monitoring of Stratospheric Gravity Waves Induced by Severe Storms. *Bulletin of the American Meteorological Society* **99**, 1813–1828 (2018).
37. Stephan, C. C. *et al.* Intercomparison of Gravity Waves in Global Convection-Permitting Models. *J. Atmos. Sci.* **76**, 2739–2759 (2019).

38. Inchin, P. A., Heale, C. J., Snively, J. B. & Zettergren, M. D. The Dynamics of Nonlinear Atmospheric Acoustic-Gravity Waves Generated by Tsunamis Over Realistic Bathymetry. *J. Geophys. Res. Space Physics* **125**, (2020).
39. Ramírez-Herrera, M. T., Coca, O. & Vargas-Espinosa, V. Tsunami Effects on the Coast of Mexico by the Hunga Tonga-Hunga Ha'apai Volcano Eruption, Tonga. *Pure Appl. Geophys.* (2022) doi:10.1007/s00024-022-03017-9.
40. Yuen, D. A. *et al.* Under the surface: Pressure-induced planetary-scale waves, volcanic lightning, and gaseous clouds caused by the submarine eruption of Hunga Tonga-Hunga Ha'apai volcano. *Earthquake Research Advances* 100134 (2022) doi:10.1016/j.eqrea.2022.100134.
41. Richter, J. H., Sassi, F. & Garcia, R. R. Toward a Physically Based Gravity Wave Source Parameterization in a General Circulation Model. *Journal of the Atmospheric Sciences* **67**, 136–156 (2010).
42. Fritts, D. C., Lund, T. S., Lund, A. C. & Yudin, V. Impacts of Limited Model Resolution on the Representation of Mountain Wave and Secondary Gravity Wave Dynamics in Local and Global Models. Part 1: Mountain Waves in the Stratosphere and Mesosphere. *JGR Atmospheres* (2022) doi:10.1029/2021JD035990.
43. O'Neill, M. E., Orf, L., Heymsfield, G. M. & Halbert, K. Hydraulic jump dynamics above supercell thunderstorms. *Science* **373**, 1248–1251 (2021).

Figure 1: **Initial Lamb wave propagation in the troposphere**: Brightness temperature changes observed by (top two rows) GOES, (bottom left) Meteosat Spinning Enhanced Visible and InfraRed Imager (SEVIRI) and (bottom right) GOES-EAST. Range rings indicate distance from Hunga Tonga in (top row) 500km and (lower rows) 2000km steps. To reduce noise from weather systems, global and antipodal panels have been processed with a 200km-radius Wiener filter, and Andes panels with a 400km boxcar and 72-km-radius Wiener filter. Black arrows indicate approximate wave location and propagation direction. All times UTC.

Figure 2: **Initial gravity wave and Lamb wave propagation at all heights:** Combined measurements of the initial wave release as observed by multiple platforms, listed with their approximate altitudes at right and at times as indicated by overlaid text labels. Inset panels showing pressure (green outline) and TEC (blue outline) distance/time series are reproduced as Extended Data Figures 1d and 3 respectively. Note that AIRS, CrIS and IASI all measure the same three stratospheric altitude channels, but only one is used here from each instrument to show all levels while maintaining visual clarity; due to the long vertical wavelengths of the observed waves, all three levels are near-identical. Airglow inset shows a northward view containing the Lamb wavefront at 09:20 UTC, ~30 minutes after the wave passed overhead. Airglow image: NSF NoirLab.

Figure 3: **Post-eruption gravity wave activity**: (a-d) in and around the volcanic plume as observed by GOES and (e-g) over the entire Pacific basin as observed by AIRS, CrIS and IASI. For (e-g) coloured labels indicate individual satellite overpass times for context, with AIRS labelled in red, CrIS in blue and IASI in purple. Note that the colour scales in panels (a) and (b) saturate significantly, and values extend to ±8K.

Extended Data Figure 1: **Eruptive energy and Lamb wave speed derived from surface pressure changes:** (a-d) Estimates of (a) Lamb-wave-induced pressure anomaly, (b) eruption explosive energy, (c) Lamb wave phase speed and (d) time of primary explosion, as computed from surface pressure data. (e) Time series of measured pressure anomaly at Broome, Australia. Data in all cases are derived from surface pressure stations, with the exception of reference values for other eruptions which are derived from Pyle (2000)[2.] Error bars on panels (a-b) are conservatively set to 0.5hPa.

Extended Data Figure 2: **Reprocessed data for the 1991 Pinatubo eruption shows evidence of gravity wave activity in the eruptive plume:** Brightness temperature measurements over the 1991 Pinatubo eruption plume, as observed by the Advanced Very High Resolution Radiometer. Phase fronts can be seen faintly in the cloud radiating from a point slightly west of Pinatubo.

Extended Data Figure 3: **Evidence of waves in the ionosphere over New Zealand and North America triggered by the Hunga Tonga eruption:** Time-distance plots of ionospheric disturbances over New Zealand and the United States, computed from GNSS-TEC perturbation data. (a) TEC perturbations as a function of distance from Hunga Tonga and time over New Zealand. (b) surface pressure at Tonga, ~60km from Hunga Tonga. (c) TEC perturbations as a function of distance and time over North America. (d) cross-section through panel (a) for selected period.

Extended Data Figure 4: **The waves generated by the eruption propagated up to the mesosphere and travelled horizontally at speeds consistent with their types:** (a) Lamb wave as observed by CIPS (centred at 24°S 309°E, 12 300 km from Hunga Tonga, and recorded 10.75 hours after the eruption). In these data, the Lamb wave is extremely close to the instrument noise floor and statistical tests were carried out to confirm that the small signal seen is consistent with the expected speed and wavelength of the Lamb wave. (b) Time-distance spectrum derived from GOES 10um channel, with Hunga Tonga located at the origin. Red solid line identifies the primary Lamb wave, red dashed lines weaker secondary Lamb waves, and yellow dashed lines outline the limits of the dispersive gravity waves in the initially-released packet.

Extended Data Figure 5: **Spectral analysis provides quantitative details of stratospheric waves generated by the eruption:** 2D S-Transform[52] (2DST) estimates of gravity wave properties measured by AIRS in a descending-node pass over the Pacific Ocean on the 15th of January 2022. (a) temperature perturbations relative to a fourth-order polynomial fit across track. (b) amplitudes estimated from these perturbations using the 2DST. (c) horizontal wavelengths estimated from these perturbations using the 2DST.

Extended Data Figure 6: **The gravity waves generated by the eruption travelled close to their maximum phase speed limit:** Expected maximum speed of a gravity wave packet relative to the observed Lamb wave, as a function of horizontal gravity wave wavelength. Blue line thickness represents the range of Lamb wave propagation speeds that we compute from AIRS, with the fast edge being approximately equal to the speed of the surface pressure signal. Orange lines represent the fast limit of gravity wave phase speeds versus horizontal wavelength, which is in the limit that the vertical wavenumber—>0. This has been calculated using the upper and lower Lamb wave speeds as the sound speed for this calculation, shown as two closely-overlaid orange lines.

Extended Data Figure 7: **Gravity waves produced by the eruption traversed the entire globe and dominated the Pacific basin following the eruption:** (a-c) transit of the leading gravity wave packet over the antipode in CrIS and AIRS 4.3 µm data (d-o) GW amplitudes over Pacific computed from AIRS, IASI and CrIS 4.3 µm data using the 2DST[37].

Extended Data Figure 8: **Surface pressure data shows evidence of multiple subsequent explosions:** Surface pressure station measurements from 04:00 – 12:00 UTC from Tonga, ~64km from Hunga Tonga. Note the multiple explosions after the initial primary Lamb wave trigger.

Extended Data Figure 9: **Water vapour observations are consistent with our proposed eruptive energy transfer mechanism:** 1x1 degree maps of IASI-B and IASI-C water vapour mixing ratio at the 2, 10 and 20hPa levels for the 15th of January 2021, using nighttime data. (a,b,c) show the data as absolute values and (d,e,f) as a difference from the local mean for January 2021. White squares indicate a lack of data due to retrieval failure, most likely due to the highly anomalous atmospheric state associated with the eruption plume.

Extended Data Figure 10: **The Lamb wave shows evidence of slowing down over South America:** Filtered data from GOES' IR channel showing the Lamb wave (strong blue/red/blue alternating lines) before (left) and after (right) passage over South America. Overlaid grey line shows the the expected location of the phase front assuming uniform progression. An increased deviation from this expected line is seen in the portion of the wave which passed over the northern half of South America.

Methods

Explosive Energy Estimate from Surface Pressure Data

We estimate the explosive energy associated with the eruption using three separate approaches. All three give a value in the range 10-28 EJ.

1. Waveform based on a nuclear explosion: Posey and Pierce (1971)[Sebastopol] suggested that the energy yield of an explosion in the atmosphere can be calculated as $E = 13p\sqrt{[r_e \sin(r/r_e)]} H_s (CT)^{3/2}$, where p is the measured pressure anomaly, r the distance from the explosion, r_e the Earth's radius, H_s the atmospheric scale height, c the speed of the wave, and T the time separation between the first and second peaks of the pressure disturbance. From available pressure-station data at distances ranging from 2500-17500 km from Hunga Tonga (Extended Data Figure 1b), this provides an estimate of ~20±8 EJ.

2. Waveform based on previous volcanic eruptions: Gorshkov (1960)[45] estimated the explosive energy of a volcanic eruption as $E = \frac{2\pi H_s \sin(\theta)}{\rho c} \int_{t1}^{t2} p^2 \, dt$, where θ is the distance from the eruption in degrees, ρ the Earth's surface air density, t is time, and t1 and t2 are the start and end times of the anomaly (different for each station). This gives an estimate of ~10EJ.

3. Estimated pressure force: assuming the pressure anomaly spreads under an even cloud of area A, then the work done by the pressure impulse over a column of height h_c is $W = pAh_c$. For an area of radius 200 km and pressure change of 5 hPa, this gives a work estimate ~18 EJ.

Estimate of Lamb Wave Phase Speed

We use the approach of Bretherton (1969)[Ashlar] and initial-release data from the European Centre for Medium-Range Weather Forecasts' Fifth-Generation Reanalysis (ERA5T) to calculate the expected speed of the Lamb wave. We first compute the local speed of sound as $c_s(z) = k\sqrt{T}$, where z is the altitude, T the local temperature and k=20.05 $\mathrm{ms^{-1}K^{-1/2}}$. For a Lamb wave, where energy density decays exponentially with height, energy density is $E(z) = C\,exp(-z/H)$, where C is a constant term which subsequently cancels in our calculation, and H is

$$H = \frac{c_s^2}{(2-\gamma)} g,$$

for a ratio of specific heats γ which we set to 1.4, and acceleration due to gravity g which we set to 9.80665$\mathrm{ms^{-1}}$. We then calculate the phase speed of the Lamb wave as a vertical mean of the speed of sound weighted by energy density, i.e.

$$c_m^2 = \frac{\int_0^\infty [c_s(z)+u(z)]^2 E(z)\, dz}{\int_0^\infty E(z)\, dz},$$

where u is the local wind speed.

For ERA5T meteorological output for the 15th of January 2022 at the 04:00 UTC timestep, this gives a phase speed of 313-318 $\mathrm{ms^{-1}}$. Similar results are obtained using the 05:00 UTC timestep. Our calculation omits the contribution of altitudes above 80 km to the energy density calculation as ERA5 data do not extend above this level, but as energy density decreases exponentially with height this contribution should be small.

Gravity Wave Speed Limit Calculation

Linear wave solutions to the Navier-Stokes equations of the form $A\ \exp[i(kx + mz - \widehat{\omega}t)]$ satisfy the dispersion relation [22] of Fritts and Alexander (2003)[5], which is fourth-order in intrinsic frequency $\widehat{\omega}$. For higher-frequency waves where $f^2 \ll \widehat{\omega}^2$ and simplifying to planar 2D propagation, i.e. $l = 0$, we can rewrite this as a fourth-order equation in intrinsic phase speed $\hat{c} = \widehat{\omega}/k$, i.e.

$$\frac{\hat{c}^4}{c_s^2} - \hat{c}^2\left(1 + \frac{1}{4H^2k^2} + \frac{m^2}{k^2}\right) + \frac{N^2}{k^2} = 0.$$

Letting $x = \hat{c}^2$ gives a quadratic form of the equation

$$ax^2 + bx + c = 0$$

where $a = 1/c_s^2$, $b = -(1 + 1/(4H^2k^2) + m^2/k^2)$ and $c = N^\wedge 2/k^\wedge 2$, with solution

$$\hat{c}^2 = \frac{-b \pm \sqrt{b^2 - 4ac}}{2a}.$$

The positive root describes acoustic wave solutions and the negative root internal gravity waves. Allowing vertical wavenumber $m \to 0$ gives the curve $\hat{c}_{max}(k)$, the maximum phase speed for gravity waves before total internal reflection would prevent their vertical propagation. This limit is

$$\hat{c}_{max}^2 = \frac{c_s^2}{2}\left[1 + (4H^2k^2)^{-1} - \sqrt{[1 + 1/(4H^2k^2)]^2 - 4N^2/(c_s^2k^2)}\right]$$

and is shown as a function of horizontal wavelength k^{-1} in Extended Data Figure 6. Our results for the wave properties produced by Hunga Tonga are consistent with previous theoretical work considering normalised full spectra of acoustic and gravity waves[46,47].

Airglow Imagery Processing

Airglow data have been obtained from the all-night cloud cameras at the Gemini Observatory on Mauna Kea, Hawaii. This assumed height layer is based on the colour of the airglow and spectral range of the cameras used at Gemini, which are both consistent with the hydroxyl (OH) airglow layer. There are five such cameras, one of which is aimed at a near-vertical angle (with a slight offset determined from study of the star field), and we use this image to identify the arrival time of the first wave packet using the image time stamp - this time is 08:48:53 UTC. At a distance of 4964 km and using an explosion time of 04:28:48 UTC, this gives a phase speed of 318.12 m/s. Further analysis using the other four cameras from the Gemini observatory gives results consistent with this.

AIRS, CRIS and IASI

We use brightness temperature observations associated with radiances in the 4.3 µm and 15 µm carbon dioxide absorption bands of AIRS, CrIS, IASI-B and IASI-C[48] on the 15th of January. These instruments can directly resolve stratospheric waves with vertical wavelengths ≳15km and horizontal wavelengths ≳30km, and typically provide twice-daily near-global coverage for each instrument in near-real time with an orbit approximately every 90 minutes. Perturbation fields suitable for spectrally and visually analysing wave signatures are produced by subtracting a fourth-order polynomial in the across-track direction from the data, consistent with previous work using these data[6,49].

CIPS

Imagery from the nadir-viewing CIPS instrument is analysed for the presence of deviations from a smooth model background of Rayleigh scattered UV sunlight (265 nm). The model removes the geometrical dependence of the observation and large-scale geophysical variability of the observed albedo. The data are binned to a uniform 7.5x7.5 km grid, allowing for observations down to 15 km horizontal wavelength. The altitude kernel limits sensitivity to vertical wavelengths $\gtrsim$10km, with a mean altitude of the contribution at ~55 km altitude. The satellite is in a sun synchronous polar orbit with an equator crossing currently near noon.

GOES/MeteoSat-SEVIRI

We use data from band 13 of GOES-EAST and GOES-WEST, and band 5 of Meteosat-SEVIRI. These instruments image the Earth's disc at a spatial resolution of 3 km (at nadir) and a temporal resolution of 10 minutes (15 minutes for SEVIRI). Raw radiance data have been converted to brightness temperatures based on the centre wavelength of the channel filters, and then differenced between adjacent timesteps to highlight wave structure.

TEC

Total electron content observations were derived from dual-frequency GPS receivers in the New Zealand GeoNet and the NOAA CORS Networks. Satellite to ground GPS signals were processed following the method of Afraimovich et al. (2000)[50], and the dTEC values are projected onto an ionospheric shell altitude of 250 km, chosen to be near the F-layer peak height[51]. The dTEC are then analysed to investigate the travelling ionospheric disturbance parameters. The data are binned onto a a 1 minute x 5 km time-distance grid; this suppresses peak values, but improves the visual clarity of the figures. All quoted TEC values are taken from these binned data, and thus slightly underestimate TEC magnitudes.

Data Availability

Airglow data are available from https://www.gemini.edu/sciops/telescopes-and-sites/weather/mauna-kea/cloud-cam/allnightlong.html. They were obtained under a Creative Commons Attribution 4.0 International License issued by the NSF's NoirLab.

AIRS and CrIS data are available from the NASA Goddard Earth Sciences Data and Information Services Center: https://disc.gsfc.nasa.gov/.

CIPS data are available from the Laboratory for Atmospheric and Space Physics at the University of Colorado Boulder: https://lasp.colorado.edu/aim/.

ERA5 data are available from the Climate Data Store, https://cds.climate.copernicus.eu.

GOES data are available from the NOAA Geostationary Satellite Server, https://www.goes.noaa.gov/.

IASI data are available from the IASI Portal, https://iasi.aeris-data.fr/.

Meteosat-SEVIRI data are available from the EUMETSAT Data Portal, https://navigator.eumetsat.int/product/EO:EUM:DAT:MSG:HRSEVIRI

Surface pressure data are archived in a Zenodo repository, doi: 10.5281/zenodo.6575810. Of the 36 pressure time series used in this study, 19 are directly included in this repository, including that shown for Tonga in Extended Data Figures 3 and 8. The repository also includes a table of phase speed estimates calculated for use in Figure 2 and Extended Data

Figure 1. A further 11 time series used to compute values in the table were obtained from existing public repositories, and the data description of the Zenodo repository specifies their locations. 6 time series from the Australian Bureau of Meteorology could not be archived due to licensing terms; from these, we have included derived estimates of phase speed in the table, and the raw data can be obtained for a fee from the Bureau of Meteorology via http://www.bom.gov.au/climate/data-services/.

TEC data are available from https://www.geonet.org.nz/ and https://geodesy.noaa.gov/CORS/.

Methods References

44. Posey, J. W. & Pierce, A. D. Estimation of Nuclear Explosion Energies from Microbarograph Records. Nature **232**, 253–253 (1971).
45. Gorshkov, G. S. Determination of the explosion energy in some volcanoes according to barograms. Bull Volcanol **23**, 141–144 (1960).
46. Yeh, K. C. & Liu, C. H. Acoustic-gravity waves in the upper atmosphere. Rev. Geophys. **12**, 193 (1974).
47. Swenson, G. R., Alexander, M. J. & Haque, R. Dispersion imposed limits on atmospheric gravity waves in the mesosphere: Observations from OH airglow. *Geophys. Res. Lett.* **27**, 875–878 (2000).
48. Hoffmann, L. et al. Intercomparison of stratospheric gravity wave observations with AIRS and IASI. Atmos. Meas. Tech. **7**, 4517–4537 (2014).
49. Alexander, M. J. & Barnet, C. Using Satellite Observations to Constrain Parameterizations of Gravity Wave Effects for Global Models. Journal of the Atmospheric Sciences **64**, 1652–1665 (2007).
50. Afraimovich, E.L. et al. Observation of large-scale traveling ionospheric disturbances of auroral origin by global GPS networks/. Earth, Planets and Space **52** 669-674 (2000)
51. Rolland, L. M. *et al.* The resonant response of the ionosphere imaged after the 2011 off the Pacific coast of Tohoku Earthquake. *Earth Planet Sp* **63**, 853–857 (2011).
52. Hindley, N. P., Smith, N. D., Wright, C. J., Rees, D. A. S. & Mitchell, N. J. A two-dimensional Stockwell transform for gravity wave analysis of AIRS measurements. Atmos. Meas. Tech. **9**, 2545–2565 (2016).

Code Availability

All software used is either already publicly available, implements equations provided in the Methods section directly, or only plots data.

Acknowledgements

CJ Wright is supported by a Royal Society University Research Fellowship, reference UF160545. CJ Wright and NP Hindley are supported by NERC grant NE/S00985X/1. MJ Alexander and CE Randall were supported by a NASA Heliophysics DRIVE Science Center (grant no. 80NSSC20K0628). CN Mitchell was supported by NERC Fellowship NE/P006450/1 for work underpinning this research. C Clerbaux and M Bouillon received funding from the European Research Council (ERC) under the European Union's Horizon 2020 and innovation programme (grant agreement No 742909, IASI-FT advanced ERC grant). J Carstens was supported by the NASA AIM Small Explorer Program, contract NAS5-03132. The Australian Institute of Marine Sciences, the Australian Bureau of Meteorology and the Tongan Met Office are thanked for provision of surface station pressure data. The authors would like to thank Isabell Krisch, Natalie Kaifler and Bernd Kaifler (all at the DLR, Oberpfaffenhofen, Germany) for assistance with preliminary data analysis, Anne Boynard (LATMOS, Paris, France) for providing the H_2O IASI data, Simon Proud (RAL) for correcting some details of the geostationary imager measurements and Ed Gryspeerdt (Imperial College, London, UK) for independent confirmation of the Lamb wave trigger time.

Author Contributions

Administration: Wright
Conceptualisation: Wright, Hoffmann, Osprey
Data curation: Hoffmann, Bouillon, Carstens, Clerbaux, Mitchell, Randall
Formal analysis: Wright, Hindley, Alexander, Barlow, Mitchell, Prata, Hoffmann
Funding acquisition: Wright, Clerbaux
Investigation: All
Methodology: Wright, Hindley, Alexander, Barlow, Mitchell, Prata, Hoffmann
Software: Wright, Hindley, Alexander, Barlow, Mitchell, Prata, Hoffmann
Visualisation: Wright, Hindley, Alexander, Barlow, Prata, Carstens, Clerbaux
Writing – original draft: Wright, Hindley, Alexander, Hoffmann, Mitchell, Prata, Carstens, Osprey
Writing - review/editing: All

Competing Interest Declaration

The authors declare no competing interests.

Additional Information

Correspondence to Corwin Wright, c.wright@bath.ac.uk.

Supplementary Data

Supplementary Figure 1: **Initial propagation of Lamb wave away from Hunga Tonga:** GOES-derived animation of initial Lamb wave release from Hunga Tonga

Supplementary Figure 2: **The Lamb wave reflected off the Andes:** GOES-derived animation showing reflection of initial Lamb wave from Andes

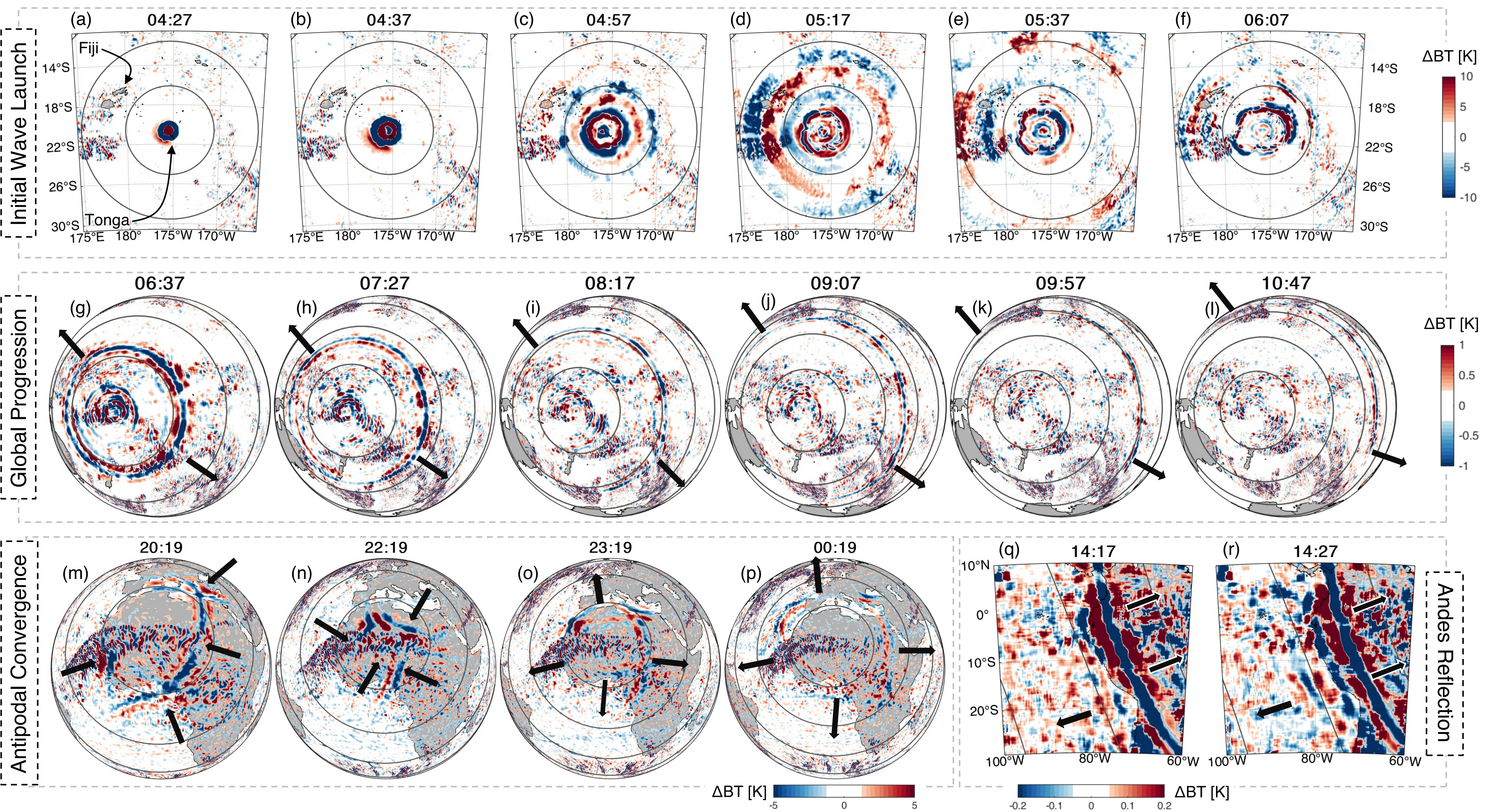
Initial Wave Launch
(a) 04:27
(b) 04:37
(c) 04:57
(d) 05:17
(e) 05:37
(f) 06:07
Fiji
Tonga
14°S
18°S
22°S
26°S
30°S
175°E 180° 175°W 170°W
ΔBT [K]
10
5
0
-5
-10
Global Progression
(g) 06:37
(h) 07:27
(i) 08:17
(j) 09:07
(k) 09:57
(l) 10:47
ΔBT [K]
1
0.5
0
-0.5
-1
Antipodal Convergence
(m) 20:19
(n) 22:19
(o) 23:19
(p) 00:19
ΔBT [K]
-5
0
5
Andes Reflection
(q) 14:17
(r) 14:27
10°N
0°
10°S
20°S
100°W 80°W 60°W
ΔBT [K]
-0.2
-0.1
0
0.1
0.2

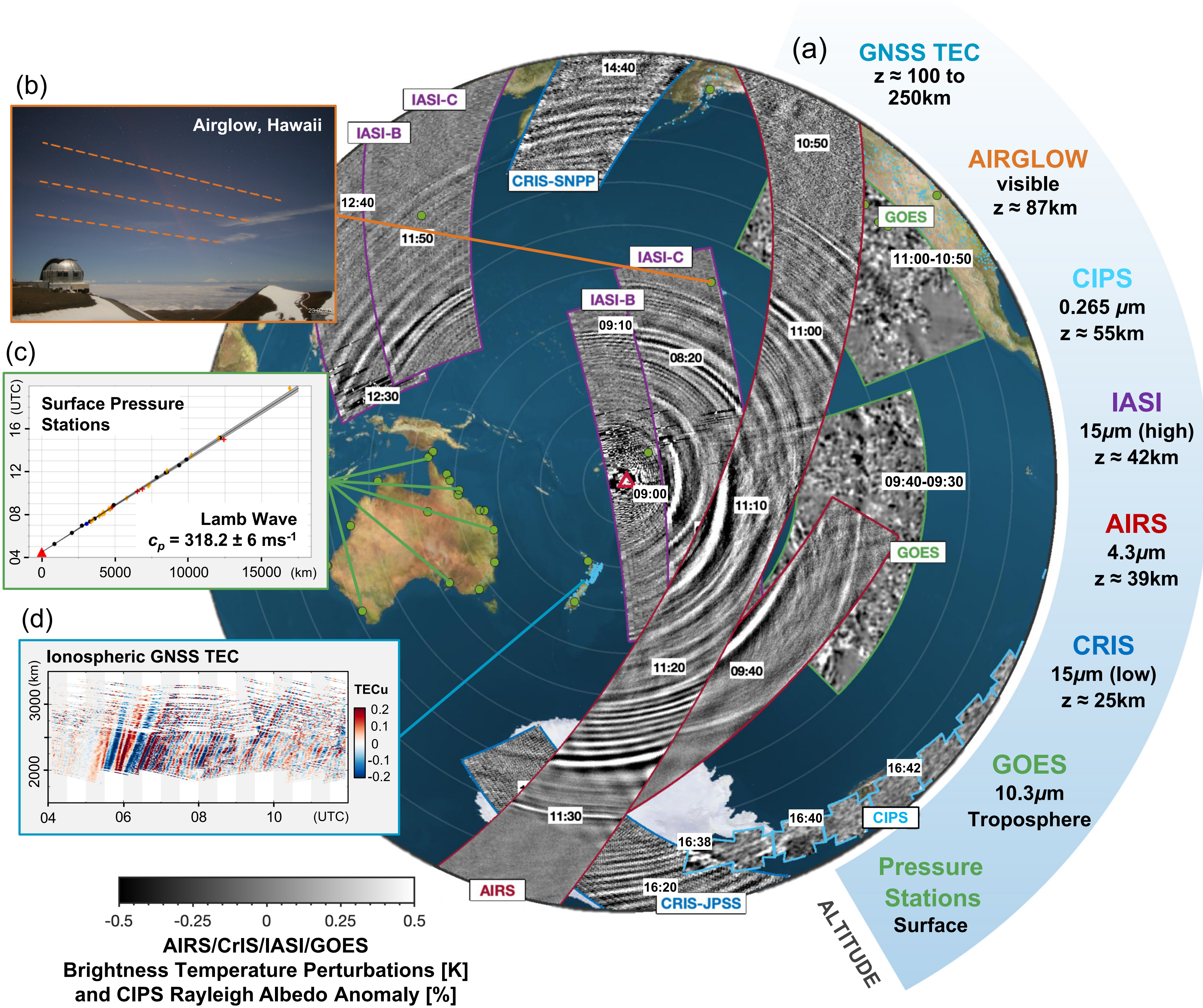

(a)
GNSS TEC
z ≈ 100 to 250km
AIRGLOW
visible
z ≈ 87km
CIPS
0.265 μm
z ≈ 55km
IASI
15μm (high)
z ≈ 42km
AIRS
4.3μm
z ≈ 39km
CRIS
15μm (low)
z ≈ 25km
GOES
10.3μm
Troposphere
Pressure Stations
Surface
ALTITUDE
IASI-C
IASI-B
CRIS-SNPP
14:40
10:50
12:40
11:50
12:30
GOES
11:00-10:50
09:10
08:20
11:00
09:00
11:10
09:40-09:30
GOES
11:20
09:40
11:30
16:42
16:40
16:38
16:20
CIPS
AIRS
CRIS-JPSS
(b)
Airglow, Hawaii
(c)
Surface Pressure Stations
Lamb Wave
c_p = 318.2 ± 6 ms^{-1}
(UTC)
04 08 12 16
0 5000 10000 15000 (km)
(d)
Ionospheric GNSS TEC
(km)
2000 3000
04 06 08 10 (UTC)
TECu
0.2 0.1 0 -0.1 -0.2
-0.5 -0.25 0 0.25 0.5
AIRS/CrIS/IASI/GOES
Brightness Temperature Perturbations [K]
and CIPS Rayleigh Albedo Anomaly [%]

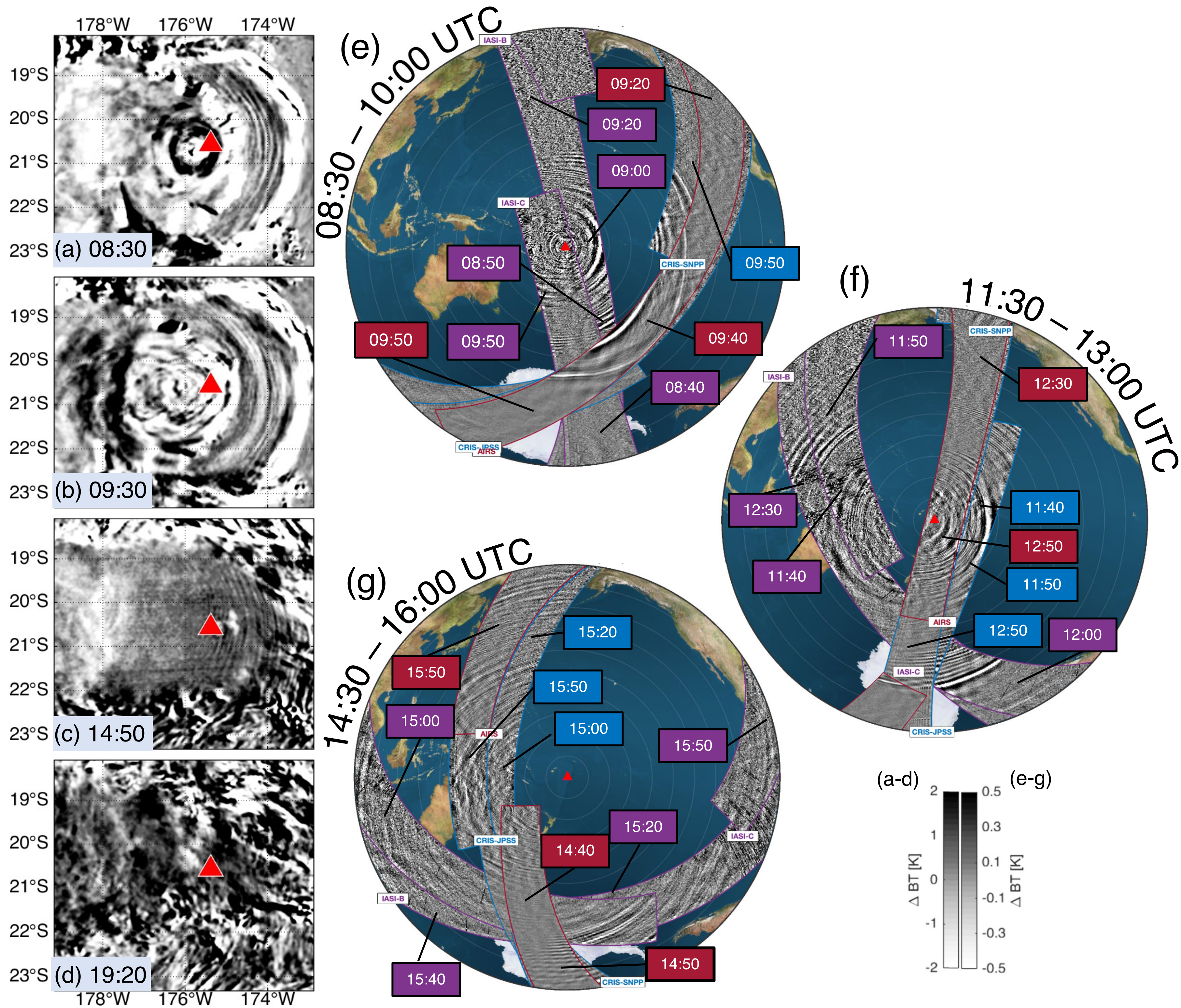

178°W
176°W
174°W
19°S
20°S
21°S
22°S
23°S
(a) 08:30
(b) 09:30
(c) 14:50
(d) 19:20
(e) 08:30 – 10:00 UTC
IASI-B
IASI-C
CRIS-SNPP
CRIS-JPSS
AIRS
09:20
09:20
09:00
08:50
09:50
09:50
09:50
09:40
08:40
(f) 11:30 – 13:00 UTC
11:50
12:30
12:30
11:40
11:40
12:50
11:50
12:50
12:00
(g) 14:30 – 16:00 UTC
15:20
15:50
15:50
15:00
15:00
15:50
15:20
14:40
15:40
14:50
(a-d)
(e-g)
Δ BT [K]
2
1
0
-1
-2
0.5
0.3
0.1
-0.1
-0.3
-0.5